Meccanica
https://doi.org/10.1007/s11012-019-01074-4

Deformation of flexible fibers in turbulent channel flow

D. Dotto · A. Soldati · C. Marchioli

Received: 13 February 2019 / Accepted: 14 October 2019

Abstract In this paper, we examine from a statistical point of view the deformation of flexible fibers in turbulent channel flow. Fibers are longer than the Kolmogorov length scale of the carrier flow and have finite inertia. Our aim is to examine the effect of local shear and turbulence anisotropy on fiber twisting and bending, when shape effects add to the inertial bias. To these aims, we use an Eulerian–Lagrangian approach based on direct numerical simulation of turbulence in dilute flow conditions. Fibers are modelled as chains of sub-Kolmogorov rods (referred to as elements hereinafter) interconnected by holonomic constraints that enable relative rotation of neighbouring elements. Statistics are computed from simulations at shear Reynolds number $\mathrm{Re}_\tau = 150$, based on the channel half height, for fibers with different aspect ratio, λ_r (defined as the ratio between the length l_r of each element r composing the fiber and its cross-sectional radius, a), and different inertia, parameterized by the Stokes number of the element, St_r. We show that bending of flexible fibers is in general stronger in the bulk of the flow, where they are subject to turbulent velocity fluctuations only. Near the wall, fibers are more easily stretched by the mean shear, especially for large-enough inertia ($St_r > 5$ in our simulations). In spite of this different dynamics, which is connected to the anisotropy of the flow, we find that the fiber end-to-end distance reaches a steady state regardless of fiber location with respect to the wall.

Keywords Direct numerical simulation · Lagrangian tracking · Wall turbulence · Flexible fibers · Deformation statistics

1 Introduction

Non-spherical particles in turbulent flow are commonly found in a number of industrial applications, from papermaking [27] and fluidised beds [4] to post-combustion soot emission [33], and environmental problems, like plankton dynamics in ocean turbulence [5, 25, 26, 32, 48], ice crystal formation in clouds [16] or atmospheric pollutant dispersion [42]. Because of this practical importance, turbulent suspensions of non-spherical particles have received a growing attention in the multiphase flow community [45]. From a modelling point of view, the description of

D. Dotto · A. Soldati · C. Marchioli
Department of Engineering and Architecture, University of Udine, 33100 Udine, Italy

A. Soldati
Institute of Fluid Mechanics and Heat Transfer, TU Wien, Getreidemarkt 9, 1060 Wien, Austria

C. Marchioli (✉)
Department of Fluid Mechanics, CISM, Piazza Garibaldi 18, 33100 Udine, Italy
e-mail: marchioli@uniud.it

Published online: 12 November 2019

such suspensions is particularly complex because of two aspects: the multiscale nature of turbulence and the strong mathematical coupling between fiber translation and fiber rotation, which depends on particle shape and orientation [10, 28–30, 36, 39, 50–52].

Most of the numerical studies dealing with non-spherical particles in turbulence focus on the case of rigid, non-deformable spheroids [10, 37, 51, 52], highlighting the tendency of fibers to align with the direction of the strongest Lagrangian fluid stretching [34, 36, 51]. In the case of inertialess spheroids, the well-known Jeffery equation [19] and its extensions to arbitrary flow fields [7, 8] and to non-axisymmetric ellipsoids [17] have been used to compute particle orbits. However, such equations cannot describe bending and twisting of long flexible fibers, whose orbits are not stable and tend to drift through orbital constants [20]. In the case of inertial spheroids, the most common numerical framework is represented by a micro-hydrodynamics approach that combines a large number of particles, with length much smaller than the flow domain, into a multi-rigid-body system [2]. The adoption of this approach for the investigation of dilute suspensions, combined with new experimental measurements [35, 41], has shed new light on the effect that particle shape and size have on inertia-driven phenomena such as preferential concentration and near-wall accumulation [29, 30, 45, 52].

Besides particle shape, however, one additional feature that is important to applications (like fiber-reinforced composite material processing [49], or hydro-entanglement processes [46], which typically occur at high Reynolds numbers) is particle flexibility: Very elongated particles with high aspect ratio, fibers in particular, may undergo significant deformation under the action of the velocity gradients that characterize the flow field around the particle. Due to the additional complexity introduced by flexibility, only a limited number of studies dealing with flexible elongated particles in turbulent dispersed flows at high Reynolds number are available. Verhille et al. [6, 15, 44] have performed experimental measurements of deformable fibers in homogeneous isotropic turbulence, focusing on different features of fiber dynamics. In particular, they examined the role of fiber inertia on the rotation rate and the role that the spatial and temporal correlations of the turbulent forcing have on the local curvature when fiber length is of the order of the integral time scale of the flow. A result that is relevant to the present study is that these correlations lead to a straightening of the fibres, which becomes more evident as fiber length increases.

Numerical simulations dealing with turbulent suspensions of flexible fibers are also scarce. Andríc et al. [2] studied the translation and re-orientation of fibers in fully-developed turbulent channel flow. Fibers longer than the Kolmogorov scale but much smaller than the flow domain were considered. It was found that fibers exhibit complex geometrical configurations during their motion, similar to conformations of polymer strands subject to thermal fluctuations. Following up on the work by Andríc et al. [2], Dotto and Marchioli [13] performed direct numerical simulations of the same flow configuration, yet considering longer simulation times (required to reach a steady state for fiber concentration), higher number of fibers (10^5 instead of 50 in the same computational domain), higher fiber-to-fluid density ratios and higher fiber length to channel height ratios. The aim of that work was to examine the effect of flexibility on fiber preferential concentration and wall accumulation, characterising from a statistical point of view the additional bias introduced by particle deformability. Another numerical study was performed by Kunhappan et al. [22] to examine the motion of flexible fibers in both homogeneous isotropic turbulence, considering flow conditions and fiber parameters close to those of [44], and channel flow turbulence, considering a 1% concentration fiber suspension. More recently, Allende et al. [1] studied the dynamics of flexible fibers passively transported in homogeneous isotropic turbulence. The authors considered the effects of both bending elasticity and flow stretching on fiber motion, and found that fibers tend to behave as stiff rods in regions of low turbulence intensity, while buckling in violent, intermittent regions. The interaction between fiber elasticity and turbulence was also examined by Rosti et al. [40]. Considering a single fiber free to move in a box of homogeneous isotropic turbulence, they were able to identify a flapping regime in which the fiber, despite its elasticity, is slaved to the turbulent fluctuations.

In the present paper, we build on the work of Dotto and Marchioli [13], and examine the deformation of inertial flexible fibers. To study this problem, we use the rod-chain model proposed by Lindström and

Uesaka [24], which extends to inertial fibers the bead-chain model originally developed by Yamamoto and Matsuoka [47] to represent the fiber as a chain of massless spherical beads that cannot detach from each other but only rotate relative to each other. The rod-chain model was also used to study paper forming [23], clustering of long flexible fibers in 2D cellular flow [31], and fiber-flow interactions and rheological properties of dilute suspensions in channel flow turbulence [2, 3].

2 Physical problem and methodology

2.1 Flow field

The physical configuration simulated in this work is a turbulent Poiseuille flow of incompressible, isothermal and Newtonian fluid in a plane channel. The governing equations, representing conservation of mass and momentum of the fluid are described by the following three-dimensional time-dependent system, written in dimensionless vector form:

$$\nabla \cdot \mathbf{u} = 0; \tag{1}$$

$$\frac{\partial \mathbf{u}}{\partial t} + \mathbf{u} \cdot \nabla \mathbf{u} = -\nabla \mathcal{P} + \frac{1}{\mathrm{Re}_\tau} \nabla^2 \mathbf{u}; \tag{2}$$

where $\mathbf{u} = (u_x, u_y, u_z)$ is the fluid velocity, $\nabla \mathcal{P}$ is the total pressure gradient that drives the flow in the streamwise direction (comprehensive of the mean and fluctuating parts), and $\mathrm{Re}_\tau = u_\tau h/\nu$ is the friction Reynolds number, with $u_\tau = (\tau_w/\rho)^{1/2}$ the friction velocity based on the mean wall shear stress τ_w and on ρ, ν the fluid viscosity and h the channel half height. We performed direct numerical simulation of these equations, imposing periodic boundary conditions in the streamwise (x) and spanwise (y) directions and no-slip conditions at the walls, z being the wall-normal direction.

2.2 Fiber tracking

Lagrangian fiber dynamics is treated in the same way as in [24, 30]. The reader is referred to these articles for a detailed description of the fiber model. Here, we provide only its main features. Each fiber is modelled as a chain of $\mathcal{N}$ rigid and inextensible elements, indexed $r \in [1, \mathcal{N}]$, having circular cross section of radius a and length l_r. Fiber elements have the same diameter and length, and are connected together through $\mathcal{N} - 1$ hinges, as shown in Fig. 1. The location of each element is given with respect to an inertial frame of reference that uses a Cartesian coordinate system, with axes defined by the base vectors $\{\mathbf{e}_x, \mathbf{e}_y, \mathbf{e}_z\}$, and origin O. Each fiber element is subject to hydrodynamic interactions, determined by the action of the drag force and torques, but also to interactions with its neighbours due to the connectivity constraint, which ensures that end-points of adjacent elements coincide.

The motion of the rth fiber element, with density ρ_r and aspect ratio $\lambda_r = l_r/a$, is governed by the following equations in vector form [24]:

$$m_r \frac{d\mathbf{v}_r}{dt} = \mathbf{F}_r^D + \mathbf{X}_{r+1} - \mathbf{X}_r; \tag{3}$$

$$\frac{d\left(\bar{\bar{\mathbf{J}}}_r \boldsymbol{\omega}_r\right)}{dt} = \mathbf{T}_r^D + \mathbf{H}_r^D + l\mathbf{o}_r \times (\mathbf{X}_{r+1} + \mathbf{X}_r); \tag{4}$$

$$\mathbf{p}_r + l_r \mathbf{o}_r - \left(\mathbf{p}_{r+1} - l_{r+1}\mathbf{o}_{r+1}\right) = \mathbf{0}\,. \tag{5}$$

In Eq. (3), $m_r = \rho_r 2\pi\lambda_r a^3$ is the mass of the element, $\mathbf{v}_r$ is the translational velocity of the element's center of mass; $\mathbf{F}_r^D$ is the hydrodynamic drag force exerted by the surrounding fluid. Terms $\mathbf{X}_{r+1}$ and $\mathbf{X}_r$ are the constraint forces produced by element $r+1$ on element r and by element r on element $r-1$, respectively.

In Eq. (4), $\bar{\bar{\mathbf{J}}}_r = \frac{m_r a^2}{12}\left[\left(4\lambda_r^2 + 3\right)\left(\bar{\bar{\boldsymbol{I}}} - \mathbf{o}_r\mathbf{o}_r^T\right) + 6\mathbf{o}_r\mathbf{o}_r^T\right]$ is the inertia tensor of the element, expressed in the inertial frame of reference O; $\mathbf{o}_r$ and $\boldsymbol{\omega}_r$ are its orientation and angular velocity, respectively; while $\bar{\bar{\boldsymbol{I}}}$ is the identity matrix. The orientation vector evolves in time according to the equation: $\dot{\mathbf{o}}_r = \boldsymbol{\omega}_r \times \mathbf{o}$. The terms $\mathbf{T}_r^D$ and $\mathbf{H}_r^D$ represent the hydrodynamic torque due to the relative spin between the fiber and the surrounding fluid, and the hydrodynamic torque due to the action of the fluid velocity gradients on the element, respectively, while $l\mathbf{o}_r \times (\mathbf{X}_{r+1} + \mathbf{X}_r)$ is the contribution of the constraint forces to the total torque. In Eq. (5), vector $\mathbf{p}_r$ represents the position of the center of mass of the rth fiber element (see also Fig. 2).

Indicating with Ψ the left-hand side of Eq. (5), the connectivity constraint can be also formulated as:

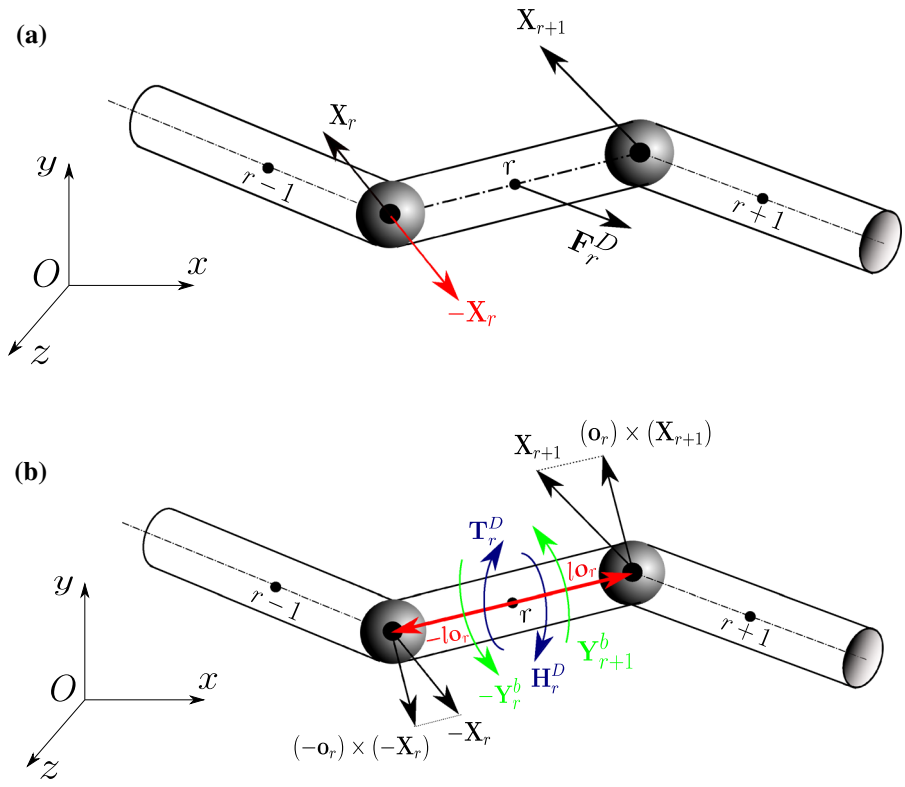

Fig. 1 Forces (**a**) and torques (**b**) applied on the r-th element of the fiber. Courtesy of Dotto and Marchioli [13]

$$\frac{d\boldsymbol{\Psi}}{dt} = \mathbf{0}\,; \tag{6}$$

with initial condition $\boldsymbol{\Psi}(t=0)=\mathbf{0}$.

Equations (3)–(5) are solved for each element of each fiber injected into the flow. The expressions used to compute the drag force and torques are selected based on the specific value of the element's Reynolds number:

$$\mathrm{Re}_{p,r} = \frac{2a}{\nu}\underbrace{\left|\left(\bar{\bar{\boldsymbol{\delta}}} - \mathbf{o}_r\mathbf{o}_r^T\right)(\mathbf{u}_r - \mathbf{v}_r)\right|}_{v_{\perp,r}}\,. \tag{7}$$

If $\mathrm{Re}_{p,r}=0$ (e.g. at the beginning of the tracking), then the analytical solution derived by Kim and Karrila [21] for an isolated axis-symmetric ellipsoid is extended to the present rod-like fiber elements by exploiting the similarity existing in shear flow between the orbiting behaviour of a rod and that of a prolate spheroid with minor axis a_{el}, major semi-axis l_{el} and aspect ratio λ_{el} [12]:

$$\frac{\lambda_{el}}{\lambda_r} = \frac{1.24}{\sqrt{\ln(\lambda_r)}} \iff a_{el} = \frac{a}{1.24}\sqrt{\ln(\lambda_r)}\,. \tag{8}$$

Even if Eq. 8 is valid for an isolated slender particle, previous studies (see e.g. [24]) have shown that the maximum error in model predictions of orbit period for rigid fibers in shear flow is below 3% for the range of aspect ratios considered here. If $\mathrm{Re}_{p,r}>0$, then inertial effects are incorporated via a suitably defined drag coefficient $C_{D,r}$, appearing in the drag force, defined as $\mathbf{F}_r^D = \bar{\bar{\mathbf{A}}}_r^D(\mathbf{u}_r - \mathbf{v}_r)$, where $\mathbf{u}_r$ is the fluid velocity evaluated at the center of mass of the fiber element and $\bar{\bar{\mathbf{A}}}_r^D$ is the resistance force tensor defined as [21]:

$$\bar{\bar{\mathbf{A}}}_r^D = \begin{cases} 6\pi\lambda_r a\mu\left[X_r^A\bar{\bar{\boldsymbol{I}}} + (Y_r^A - X_r^A)\mathbf{o}_r\mathbf{o}_r^T\right] & \text{if } \mathrm{Re}_{p,r}=0\,; \\ 2C_{D,r}\rho\lambda_r a^2 v_{\perp,r}\left(\bar{\bar{\boldsymbol{I}}} - \mathbf{o}_r\mathbf{o}_r^T\right) & \text{if } \mathrm{Re}_{p,r}>0\,. \end{cases} \tag{9}$$

The coefficients X_r^A and Y_r^A are defined as in [13, 21] and are not reported here for sake of brevity. The

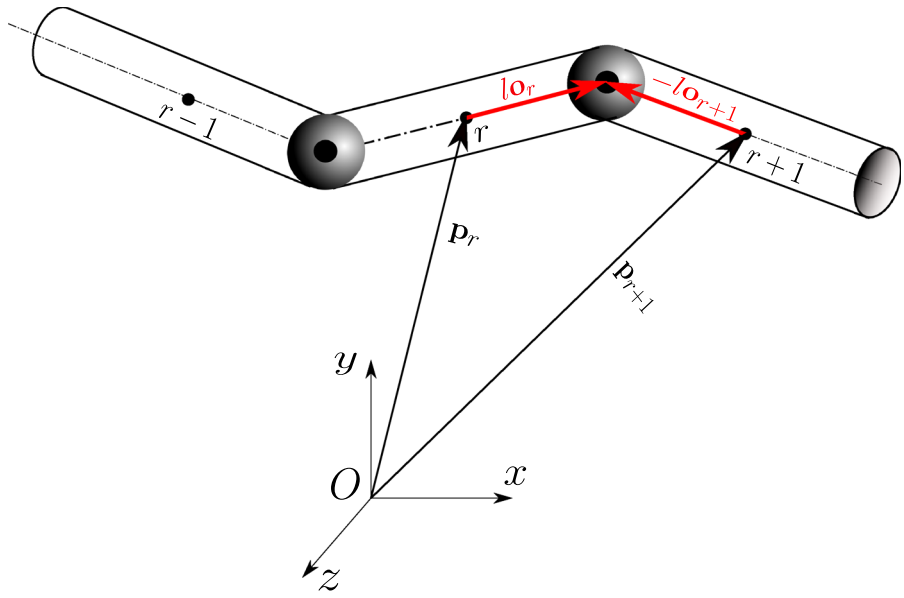

Fig. 2 Inextensibility cinematic constraint applied to the elements r and $r+1$ of the fiber. Courtesy of Dotto and Marchioli [13]

coefficient $C_{D,r}$ is computed using the following expressions [11, 13]:

$$C_{D,r} = \begin{cases} C^I_{D,r} = 9.689\mathrm{Re}_{p,r}^{-0.78} & \text{if } \mathrm{Re}_{p,r} \in]0, 0.1]\,; \\ C^I_{D,r}\left(1 + 0.147\mathrm{Re}_{p,r}^{0.82}\right) & \text{if } \mathrm{Re}_{p,r} \in]0.1, 5]\,; \\ C^I_{D,r}\left(1 + 0.227\mathrm{Re}_{p,r}^{0.55}\right) & \text{if } \mathrm{Re}_{p,r} \in]5, 40]\,; \\ C^I_{D,r}\left(1 + 0.0838\mathrm{Re}_{p}^{0.82}\right) & \text{if } \mathrm{Re}_{p,r} \in]40, 400]\,; \\ 1 & \text{if } \mathrm{Re}_{p,r} > 400\,. \end{cases} \tag{10}$$

The hydrodynamic torque is computed as $\mathbf{T}^D_r = \bar{\bar{\mathbf{C}}}^D_r(\boldsymbol{\Omega}_r - \omega_r)$, where $\bar{\bar{\mathbf{C}}}^D_r$ is the resistance torque tensor, defined as [21]:

$$\bar{\bar{\mathbf{C}}}^D_r = \begin{cases} 8\pi\lambda_r^3 a^3 \mu \left[X^C_r \bar{\bar{\boldsymbol{I}}} + (Y^C_r - X^C_r)\mathbf{o}_r\mathbf{o}_r^T \right] & \text{if } \mathrm{Re}_{p,r} = 0\,; \\ \frac{2}{3} C_{D,r}\rho\lambda_r^3 a^4 v_{\perp,r}\left(\bar{\bar{\boldsymbol{I}}} - \mathbf{o}_r\mathbf{o}_r^T\right) & \text{if } \mathrm{Re}_{p,r} > 0\,; \end{cases} \tag{11}$$

where the coefficients X^C_r and Y^C_r are defined as in [13, 21] and are not reported here for sake of brevity. The torque due to the velocity gradients at the center of mass of each fiber element is defined as:

$$\bar{\bar{\mathbf{H}}}^D_r = \begin{cases} -8\pi\mu a^3 \lambda_r^3 Y^H_r \left(\bar{\bar{\boldsymbol{\varepsilon}}}\mathbf{o}_r\right) : \left(\dot{\bar{\bar{\gamma}}}_r \mathbf{o}_r\right) & \text{if } \mathrm{Re}_{p,r} = 0\,; \\ -\frac{2}{3} a^4 \lambda_r^3 C_{D,r}\rho v_{\perp,r}\left(\bar{\bar{\boldsymbol{\varepsilon}}}\mathbf{o}_r\right) : \left(\dot{\bar{\bar{\gamma}}}_r \mathbf{o}_r\right) & \text{if } \mathrm{Re}_{p,r} > 0\,; \end{cases} \tag{12}$$

where Y^H_r is defined as in [13, 21], $\bar{\bar{\boldsymbol{\varepsilon}}}$ is the Levi-Civita tensor, $\dot{\bar{\bar{\gamma}}}_r$ is the velocity gradient tensor, and the operator : is defined such that:

$$\left(\bar{\bar{\boldsymbol{\varepsilon}}}\mathbf{o}_r\right) : \left(\dot{\bar{\bar{\gamma}}}_r \mathbf{o}_r\right)\Big|_i = \varepsilon_{ijk}\left(\dot{\gamma}_{jl,r} o_{l,r}\right) o_{j,r}.$$

Details on the $\mathcal{LU}$ factorization used to solve the tridiagonal block-matrix system associated to the constraint equation are given in [13], where a discussion on the limitations of the model and its suitability in the limit of dilute flow (not repeated here for sake of brevity) can also be found.

2.3 Summary of simulations

Simulations are carried out at $\mathrm{Re}_\tau = 150$, with $u_\tau = 0.1177$ m/s. The corresponding bulk Reynolds number, for the case of air, is $\mathrm{Re}_b = u_b h/\nu = 2250$, where $u_b = 1.77$ m/s is the bulk velocity. The Reynolds number based on the hydraulic diameter is $\mathrm{Re}_D \simeq 9000$. The size of the computational domain is $L_x = 1885 \times L_y = 942 \times L_z = 300$ wall units (*i.e.* in

terms of variables identified with the superscript "+" made dimensionless using ν and u_τ), discretized with $128 \times 128 \times 129$ grid nodes. The non-dimensional step for time integration is 0.003 in wall units.

Equations (1)–(2) are discretized using a pseudo-spectral method based on transforming the field variables into the wavenumber space, through a Fourier representation for the periodic directions x and y, and a Chebychev representation along z. A two-level explicit Adams-Bashfort scheme for the non-linear terms and an implicit Crank–Nicolson method for the viscous terms are employed for the time advancement. The convective non-linear terms are first computed in the physical space and then transformed in the wavenumber space using a de-aliasing procedure based on the 2/3-rule; derivatives are evaluated directly in the wavenumber space to maintain spectral accuracy. The equation for the orientation vector $\mathbf{o}_r$ is integrated in time using a standard 4th-order Runge-Kutta scheme, while Eqs. (3)–(5) are solved using a mixed explicit/implicit differencing procedure developed by [14]. The same time step size as that of the fluid is used for integration, and the total Lagrangian tracking time in wall units is $t^+ = t\nu/u_\tau^2 = 1250$, which was enough to reach the steady state in fiber wall-normal concentration. The relevant parameters for time integration are a, λ_r and the Stokes number of the fiber element [43]:

$$St_r = \frac{2a^2 S}{9\nu} \frac{\lambda_r \ln(\lambda_r + \sqrt{\lambda_r^2 - 1})}{\sqrt{\lambda_r^2 - 1}} \frac{{u_\tau}^2}{\nu}. \tag{13}$$

The different Stokes numbers considered in this study, together with the main simulation parameters characterising the different fiber sets, are given in Table 1. The Stokes number relative to the entire fiber in its fully-stretched configuration, St_f (equivalent to the Stokes number of a rigid fiber with equal density and total length $L_f = \mathcal{N} \cdot l_r$), and the different ratios of fiber density to fluid density, $S = \rho_r/\rho$, are also shown. All fibers have the same dimensionless radius $a^+ \simeq 0.17$, corresponding to $a \simeq 11.8$ μm for gas-solid flow. To ensure converged statistics, swarms of $M = 10^5$ fibers, each having $\mathcal{N} = 7$ elements (as in [2]), are tracked for each combination of values in the (λ_r, St_r) space.

In the present channel flow, the Kolmogorov length scale has a mean value $\eta^+_{K,avg} \simeq 2$, and varies from $\eta^+_{K,min} \simeq 1.62$ at the wall to $\eta^+_{K,max} \simeq 3.61$ at the channel center [38]. Therefore, individual fiber elements are smaller (or not longer, at least) than the smallest scale in the flow, but the entire fiber is longer regardless of λ_r. This implies that fiber elements will experience slightly different local flow conditions (velocity fluctuations and gradients) with respect to their neighbours [39]: Our model takes these differences into account, and reproduces their effect on the overall translational and rotational dynamics of the fiber.

Table 1 Summary of the simulation parameters relative to the fibers

St_r	St_f	λ_r	l_r^+	l_r [μm]	L_f^+	L_f/h	S
1	2.2	2	0.67	46.3	4.7	0.032	102.4
	1.8	5	1.68	116.0	11.8	0.079	66.5
5	11.0	2	0.67	46.3	4.7	0.032	512.0
	9.1	5	1.68	116.0	11.8	0.079	322.8
30	64.9	2	0.67	46.3	4.7	0.032	3071.8
	54.5	5	1.68	116.0	11.8	0.079	1996.5

The length of a fiber element is given both in wall units (l_r^+) and in dimensional units (l_r, microns). The length of the entire fiber is given in wall units (L_f^+) and as a function of the channel half height (L_f/h)

3 Results and discussion

In this section, we provide a statistical characterization of fiber deformation inside the channel. Figure 3 provides qualitative visualizations of the instantaneous distribution of the $St_r = 5$ fibers with $\lambda_r = 5$ in two different fluid slabs at time $t^+ = 900$ of the simulation. Fibers start as fully-stretched (all fiber elements are aligned) at random position and with random orientation, and attain a non-homogeneous distribution that is biased by fiber inertia. Our aim is to characterize from a statistical point of view fiber bending at varying fiber elongation and inertia. Fibers with different length (namely aspect ratio) and different inertia (namely Stokes number) will respond selectively to the fluid velocity gradients acting at spatially-changing locations along the fiber.

Note that, in the present simulations, fibers have zero flexural rigidity and therefore do not have a unique equilibrium conformation (minimal energy

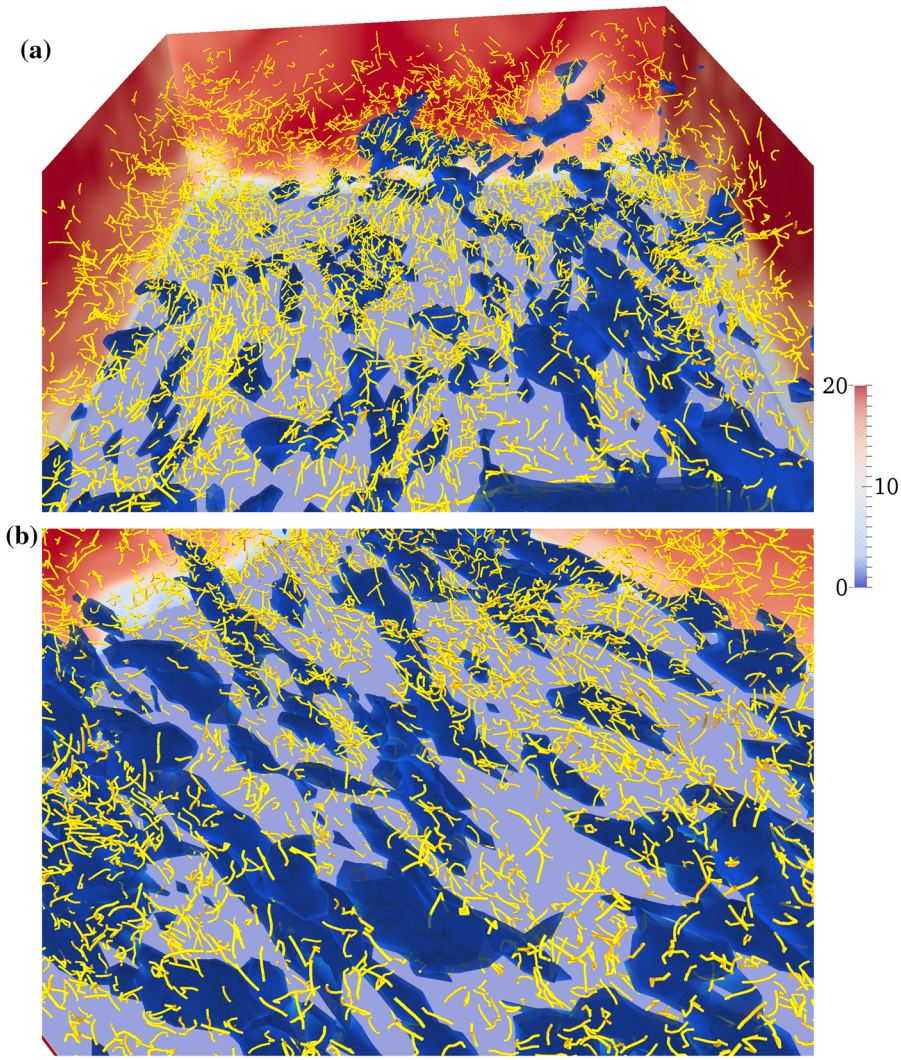

Fig. 3 Instantaneous distribution of $St_r = 5$ fibers with $\lambda = 5$ in turbulent channel flow. In **a**, only fibers in the slab $698 < x^+ < 1306$, $297 < y^+ < 705$, $0 < z^+ < 150$ are shown. The close-up view in **b** refers to a smaller portion of the flow domain ($698 < x^+ < 1021$, $297 < y^+ < 559$, $0 < z^+ < 120$). The colormap at the side of the two snapshots shows the streamwise fluid velocity distribution (red: higher-than-mean velocity, blue: lower-than-mean velocity). Flow structures are visualised using the Q-criterion [18]: Isosurfaces correspond to $Q = -0.05$

conformation). In fact, all conformations attained by the fibers are equivalent from an energy point of view.

One observable that can be examined to characterize bending is the solid angle α between two neighbouring fiber elements: $\alpha = 0$ corresponds to a fully-stretched fiber in which elements have the same orientation, whereas bending is associated with positive values of α (the stronger the bending, the higher the value of α). We thus start our analysis by examining the PDF of the solid angle, $\langle\alpha\rangle$, shown in Fig. 4. Brackets indicate averaging over the six values of α that can be calculated considering all pairs of neighbouring elements in one fiber. PDFs are time-averaged and conditioned to the location of the fibers in the wall-normal direction. In particular, we considered two sub-sets: Fibers with instantaneous distance from the wall smaller than 5 times the viscous sublayer thickness, δ_{SV}, and those with distance larger than $20\delta_{SV}$, corresponding to a fluid slab of thickness $10\delta_{SV}$ in the channel center.

In the $St_r = 1$ case (Fig. 4a), we observe that fibers in the near wall region sample rather uniformly all possible values of the solid angle, for both $\lambda_r = 2$ (solid line) and $\lambda_r = 5$ (dashed line): there is a smooth peak at $\langle\alpha\rangle \simeq 1$ and a smooth decay around this peak. Fibers in the center of the channel (filled circles for $\lambda_r = 2$, filled squares for $\lambda_r = 5$) sample roughly the same angles $\langle\alpha\rangle$, but their PDF exhibits a more irregular shape: there is a relative minimum at $\langle\alpha\rangle \simeq 0.7$ and a sharp peak at $\langle\alpha\rangle \simeq 1$. We remark here that a

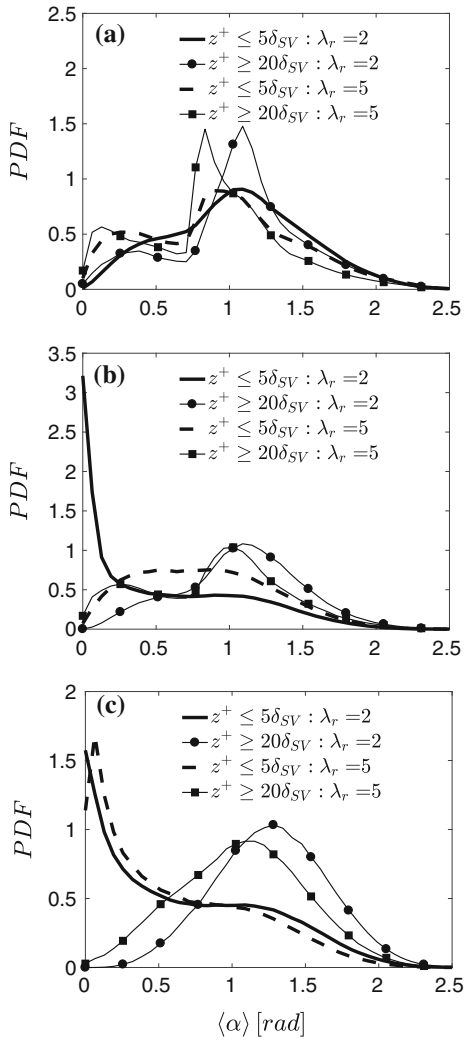

Fig. 4 PDF of the solid angle, $\langle\alpha\rangle$, conditioned to fiber location. Lines represent the PDF of fibers instantaneously located within a distance $z^+ = 5\delta_{SV}$ from the wall, symbols represent the PDF of fibers instantaneously located in the channel centre ($z^+ \geq 20\delta_{SV}$). **a** $St_r = 1$; **b** $St_r = 5$; **c** $St_r = 30$

uniform distribution of angles would correspond to the value $\langle\alpha\rangle \simeq 1.2$. Therefore, Fig. 4a suggests that $St_r = 1$ fibers are characterized (on average) by a rather uniform distribution of deformations, regardless of their location within the flow.

In the $St_r = 5$ case (Fig. 4b), we still find a preferential sampling for values of $\langle\alpha\rangle$ that correspond to a statistically uniform distribution of deformations, but only for the subset of fibers in the center of the channel. A more complex behaviour is observed for the fibers in the near-wall region: As indicated by the sharp peak of the PDF, shorter fibers ($\lambda_r = 2$, solid line) sample preferentially angles close to $\langle\alpha\rangle = 0$ that correspond to the fully-stretched conformation. No such peak is found for the more elongated fibers ($\lambda_r = 5$, dashed line), which are characterized by a positively skewed PDF. This different behaviour can be ascribed to the different tendency of the $St_r = 5$ fibers to accumulate at the wall at varying length, not discussed here but shown in [13]: The $\lambda_r = 2$ fibers develop a peak of concentration inside the viscous sublayer, where they can be more easily stretched by mean shear while being subject to low turbulent velocity fluctuations; the $\lambda_r = 5$ fibers develop a peak of concentration just outside the viscous sublayer and are exposed to weaker shear and higher velocity fluctuations, which act to buckle interconnected elements. We remind that, for a given value of St_r, the fiber-to-fluid density ratio decreases with λ_r so shorter fibers have higher inertia (see also Table 1). In the $St_r = 30$ case (Fig. 4c), the PDFs become less sensitive to changes in fiber elongation. Fibers in the center of the channel are characterized by a quasi-Gaussian distribution, indicating uniform distribution of deformations especially for the $\lambda_r = 2$ case; fibers in the near-wall region are characterized by a clear preferential sampling of small or zero values of the solid angle, indicating strong stretching.

The trends just discussed for the solid angle can be naturally correlated with the mean shear rate acting on the fibers, especially in the near-wall region. To quantify this correlation, in Figs. 5, 6 and 7, we show the scatter plots of the solid angle, $\langle\alpha\rangle$, as a function of the spanwise vorticity, $\Omega_{y,G}$, sampled at the fiber's center of mass, G. Both values of the aspect ratio are considered here, and scatter plots are conditioned to fiber location with respect to the wall: the top panels in Figs. 5, 6 and 7 were obtained by counting only the fibers instantaneously located inside the near-wall fluid slab of thickness $5\delta_{SV}$; while the fibers in the centre of the channel ($z^+ \geq 20\delta_{SV}$) were used to compute the plots in the bottom panels. We remind that, close to the wall, $\Omega_{y,G}$ is nearly equal to the mean shear, $\mathrm{d}u/\mathrm{d}z$. The colormap shows low correlation in blue and strong correlation in red, with values ranging from 0 to 1 upon normalisation by the total number of fibers counted. At lower inertia ($St_r = 1$, Fig. 5), we observe a persistent correlation between values of $\langle\alpha\rangle$ close to unity, corresponding to the peak of the PDFs

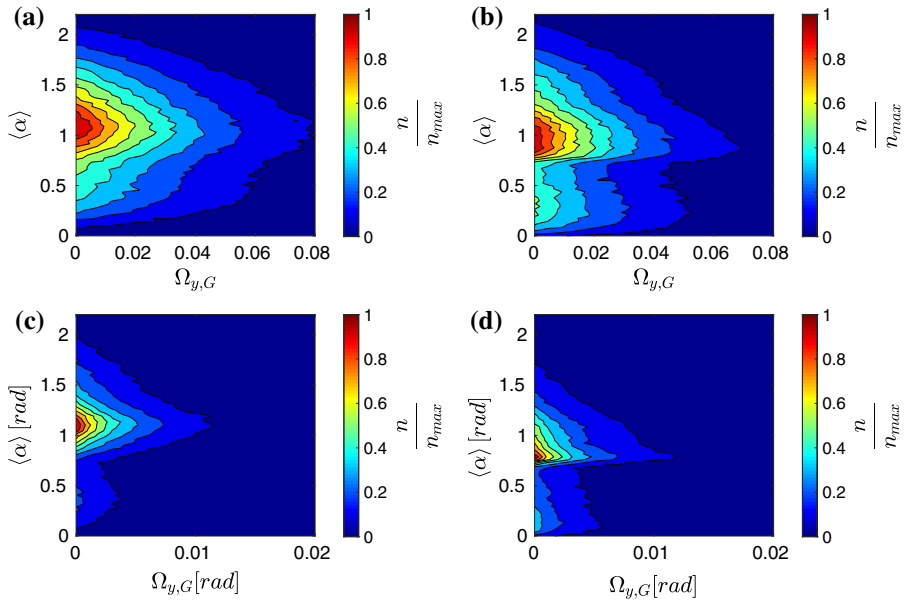

Fig. 5 Scatter plot of the solid angle, $\langle\alpha\rangle$, versus the fluid spanwise vorticity, $\Omega_{G,y}$, conditionally sampled at the $St_r = 1$ fiber position. Upper panels refer to the near-wall region, lower panels related to the bulk region; left $\lambda_r = 2$, right $\lambda_r = 5$

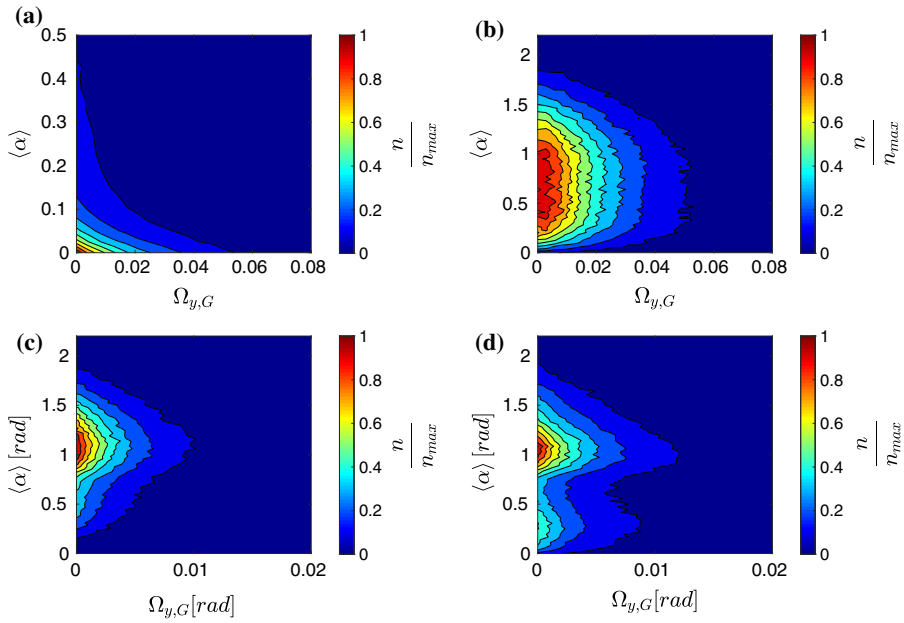

Fig. 6 Scatter plot of the solid angle, $\langle\alpha\rangle$, versus the fluid spanwise vorticity, $\Omega_{G,y}$, conditionally sampled at the $St_r = 5$ fiber position. Upper panels refer to the near-wall region, lower panels related to the bulk region; left $\lambda_r = 2$, right $\lambda_r = 5$

in Fig. 4), and a wide range of near-wall values of $\Omega_{G,y}$, as shown in the top panels of Fig. 5. For the fibers in the center of the channel, the correlation is still maximum at $\langle\alpha\rangle \simeq 1$ yet for values of $\Omega_{G,y}$ that are much smaller than those sampled near the wall, as shown in the bottom panels of Fig. 5. The behaviour of the PDFs implies that the effect of shear on low-inertia fibers is not strong enough to overcome the effect of the smallest flow scales (which acts to deform the fibers and is only partially filtered out by their inertia at low Stokes number) and induce significant stretching in the wall proximity. At intermediate inertia ($St_r = 5$, Fig. 6), the scatter plot in the near-wall region (top panels) changes significantly with fiber elongation: For the $\lambda_r = 2$ fibers (Fig. 6a), the most evident correlation is found for relatively high values of $\Omega_{G,y}$ but small values of $\langle\alpha\rangle$ for the $\lambda_r = 2$ fibers (Fig. 6a). On the other hand, for the $\lambda_r = 5$ fibers (Fig. 6b), the

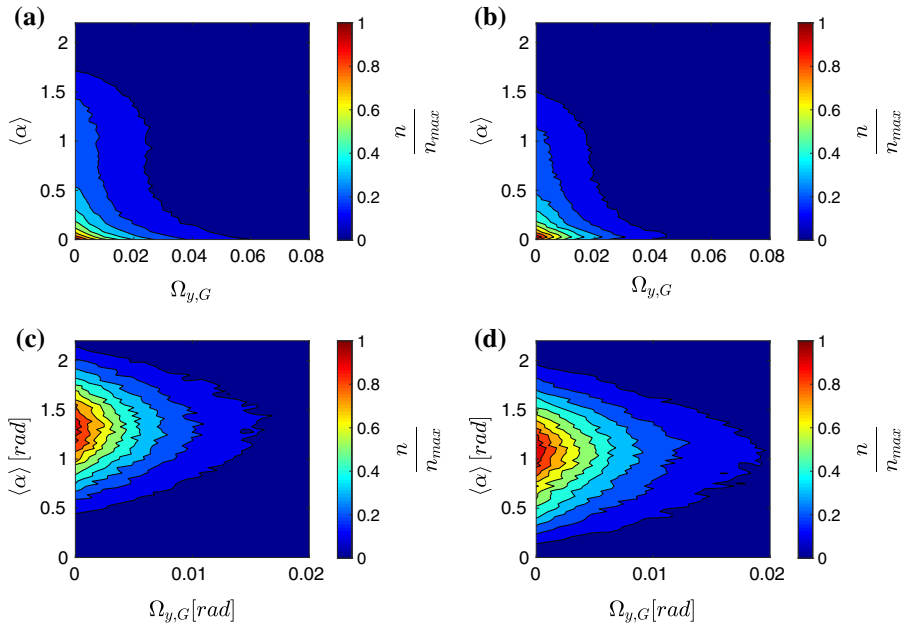

Fig. 7 Scatter plot of the solid angle, $\langle\alpha\rangle$, versus the fluid spanwise vorticity, $\Omega_{G,y}$, conditionally sampled at the $St_r = 30$ fiber position. Upper panels refer to the near-wall region, lower panels related to the bulk region; left $\lambda_r = 2$, right $\lambda_r = 5$

correlation is high for high values of $\langle\alpha\rangle$. In the center of the channel (Fig. 6c, d), fibers sample low values of spanwise vorticity regardless of their aspect ratio and highest correlations are found for $\langle\alpha\rangle$ just above unity. Overall, the strongest correlations are always found for values of the solid angle that correspond to peaks in the PDFs of Fig. 5b). At high inertia ($St_r = 30$, Fig. 7), scatter plots are not much affected by aspect ratio anymore. In the near-wall region (top panels), fibers are stretched in regions of high vorticity (mean shear). In the center of the channel (bottom panels), fibers undergo bending in the regions of low vorticity characterized by nearly isotropic and homogeneous turbulent flow conditions.

To further quantify bending, we consider next a different observable: The fiber end-to-end distance, L^+, defined as the three-dimensional distance between the end points of the fiber. When the fiber is fully elongated, the end-to-end distance is equal to the fiber length, L_f^+; when the end-to-end distance is zero, the two end points of the fiber touch each other; intermediate values indicate bending and buckling of neighbouring elements. This observable was also examined by Verhille et al. [9, 15] for fibers much longer than those considered here and for a different flow configuration (homogeneous isotropic turbulence). Figure 8 shows the time evolution of the mean end-to-end distance, averaged over all fibers in the flow domain and in time (over the last 350 viscous time units of the simulation). Insets labeled with d), e) and f) show the same time evolution when L^+ is normalised by L_f^+. As done before, the statistics is conditioned to fiber position to highlight the effect of flow anisotropy. The length of a fully-stretched fiber, represented by the thin horizontal lines in Fig. 8, is $L_f^+ = 4.7$ for fibers with $\lambda_r = 2$ and $L_f^+ = 11.8$ for fibers with $\lambda_r = 5$: Dotto and Marchioli [13] have shown that the region of largest stretching, namely largest L^+, correlates well with the region of maximum turbulent Reynolds stress and that the strength of this correlation depends on inertia, as well as on elongation since longer fibers appear to get stretched closer to the wall than shorter ones.

Starting from the initial time step of the simulations (in which the fibers are fully stretched) we first observe, for all fiber sets and regardless of fiber location, a transient during which L^+ decreases followed by a steady state characterized by a constant value of L^+. In this respect, the dynamical properties of our fibers are clearly different from those of elastic fibers, like those considered by Rosti et al. [40], which were found to obey a flapping regime characterized by fiber oscillations completely determined by the turbulent flow field. This difference stems from the fact that they considered fibers with length in the inertial range of scales that are allowed to stretch under the action of

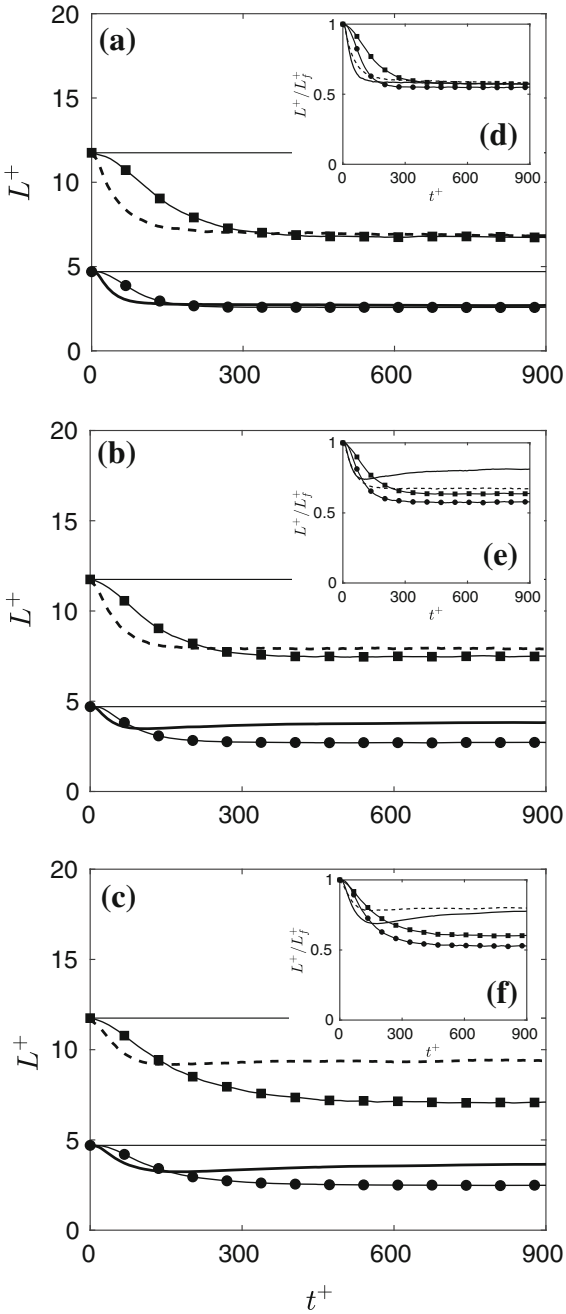

Fig. 8 Time evolution of the dimensionless fiber end-to-end distance, L^+: **a** $St_r = 1$; **b** $St_r = 5$; **c** $St_r = 30$. The insets in each panel show the time evolution of the ratio L^+/L_f^+. Lines and symbols are follows: ——$z^+ \leq 5\delta_{VS}$ and $\lambda_r = 2$; –●–$z^+ \geq 20\delta_{VS}$ and $\lambda_r = 2$; - - -$z^+ \leq 5\delta_{VS}$ and $\lambda_r = 5$; –■–$z^+ \geq 20\delta_{VS}$ and $\lambda_r = 5$

the fluid velocity gradients. In general we see that our inextensible fibers reach the steady state condition earlier in the near-wall region (lines) rather than in the center of the channel (symbols). Also, fibers with lower aspect ratio reach the steady state earlier than those with higher aspect ratio, especially at low inertia. In the $St_r = 1$ case (Fig. 8a), the steady state value of L^+ for the fibers in the near-wall region is the same for the fibers in the center of the channel, regardless of their distance from the wall and regardless of λ_r. The inset 8d) shows that the steady state value of L^+ is approximately equal to $0.6L_f^+$, in agreement with the findings of [13]. In the near-wall region, such steady state is reached at $t^+ \simeq 75$ by the shorter fibers (solid line) and at $t^+ \simeq 150$ by the longer fibers (dashed line). In the channel center, the steady state is reached at $t^+ \simeq 150$ by the shorter fibers (circles) and at $t^+ \simeq 300$ by the longer fibers (squares). In the $St_r = 5$ case (Fig. 8b), the steady state value of L^+ is higher for the fibers in the near-wall region, especially for $\lambda_r = 2$, indicating lower bending. The inset 8e) shows that the steady state value of L^+ changes significantly with the aspect ratio λ_r. The trend highlighted by Fig. 8b becomes more evident for the high-inertia fibers, as can be seen in Fig. 8c. For these fibers, the inset 8e shows that the steady state value of L^+ is less dependent on λ_r and more sensitive to the position of the fiber with respect to the wall. The results shown in Fig. 8 indicate that mean fiber deformation is characterized by an initial transient during which fibers adapt to the local flow conditions and "forget" about the imposed initial condition. This transient is generally shorter in the near-wall region because of the persistent action of the mean shear, while fibers in the bulk of the flow are subject to a nearly delta-correlated flow field, in both space and time. Eventually, a steady state is always reached, and the effect of flow anisotropy on mean deformation is felt only at sufficiently-high fiber inertia ($St_r \geq 5$ in the present simulations). We remark that the time evolution of the end-to-end distance is the same as that of the fluid velocity fluctuations (not shown), especially at low fiber inertia [13]. This indicates a clear connection between the local flow conditions experienced by the fibers and their deformation, an observation that is in qualitative agreement with the findings of Verhille et al. [6, 15, 44]. The correlation weakens as fiber inertia increases, indicating that bending dynamics is not much affected by the

instantaneous turbulent flow but, rather, by its time-persistent features, as the mean shear experienced by fibers upon accumulating in the near-wall region.

The bending dynamics observed so far and the effect of the fluid velocity gradients on fiber deformation can be interpreted by means of the constraint forces generated within the fiber, which are a direct outcome of the Lagrangian tracking. The components parallel and orthogonal to the major symmetry axis of the r-th fiber element are defined, in terms of modulus, as $|\mathbf{X}_r \cdot \mathbf{o}_r|$ (tensile force) and $|\mathbf{X}_r \times \mathbf{o}_r|$ (bending force), respectively. The behaviour of these two components along the wall-normal direction of the channel is shown in Fig. 9, where profiles refer to force components that were averaged over the last 350 viscous time units of the simulation. Starting from the wall, and moving towards the center of the channel, we notice an increase of both force components until a peak is reached: The location of the peak almost coincides with the location at which fiber concentration reaches a maximum and the momentum transferred by the fluid to the fibers is also maximum [13]. Beyond this peak, the curves decrease monotonically and reach a plateau that is maintained all the way to the channel center. Longer fibers (dashed lines) are characterized by higher values of both tensile and bending force compared to shorter fibers (solid lines). We also observe that the magnitude of the constraint force components is proportional to fiber inertia: As the Stokes number increases, constraint forces also increase, spanning more than one order of magnitude going from $St_r = 1$ to $St_r = 30$. This clearly indicates

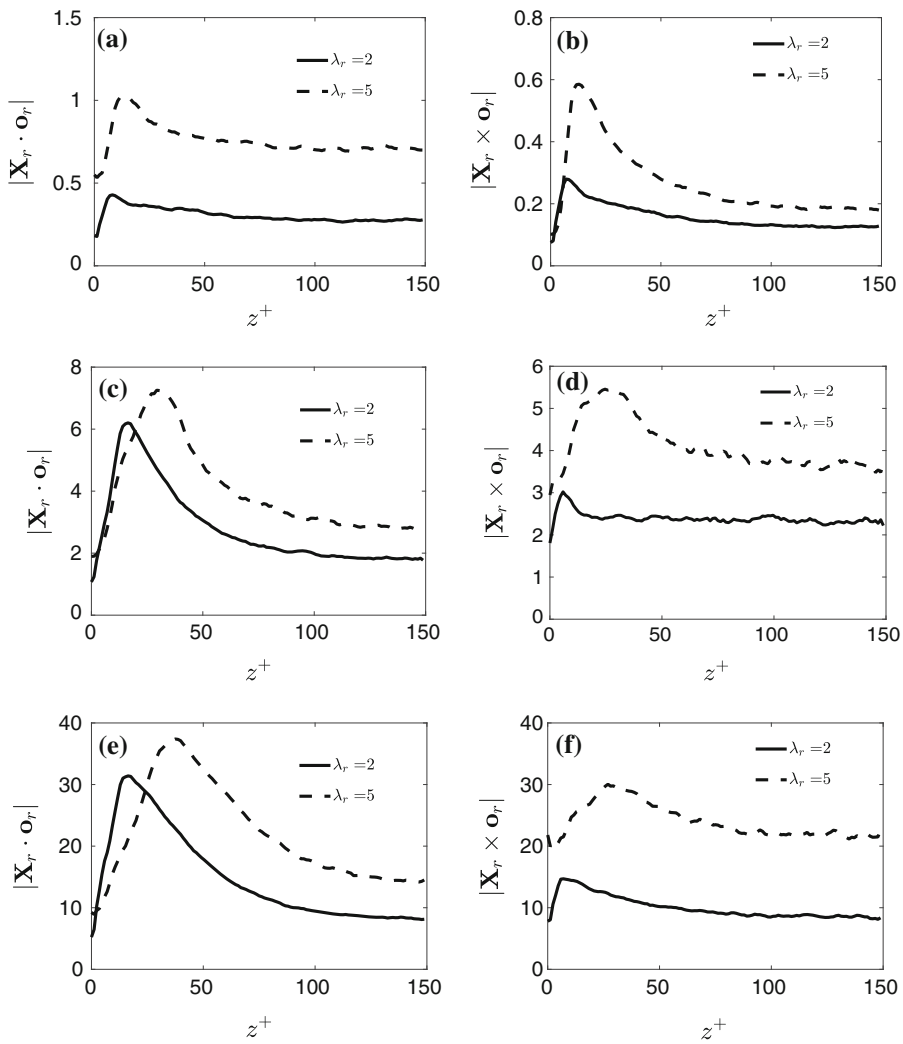

Fig. 9 Constraint forces acting on the fibers: Axial component, $|\mathbf{X}_r \cdot \mathbf{o}_r|$ (left-hand panels), and orthogonal component, $|\mathbf{X}_r \times \mathbf{o}_r|$ (right-hand panels), with respect to the major symmetry axis of the fiber. **a**, **b** $St_r = 1$; **c**, **d** $St_r = 5$; **e**, **f** $St_r = 30$

that elements belonging to longer fibers and/or high-inertia fibers exhibit a stronger tendency towards relative translation and bending of their major symmetry axis. The role played by the aspect ratio can be easily explained by considering that longer fibers sample instantaneously regions of different fluid velocities and velocity gradients, which in turn determine a stronger influence of one fiber element on translation and rotation of the other fiber elements.

4 Conclusions and future developments

In this work, we have provided a statistical characterization of the bending dynamics of inertial flexible fibers dispersed in turbulent channel flow. The motion of the fibers was simulated numerically, using an Eulerian-Lagrangian approach based on direct numerical simulation of turbulence and Lagrangian fiber tracking. The rod-chain model of Lindström and Uesaka [24] was adopted and results obtained for different values sampling the (λ_r, St_r) space have been presented. The most general feature we could observe is that fibers are stretched by mean shear in the near-wall region, while retaining a more deformed conformation in the centre of the channel. Fiber deformation is affected by flow anisotropy and fiber inertia, which determine a different time evolution of the three-dimensional end-to-end distance, used here to quantify fiber bending. Differences are more evident for fibers with higher inertia, but never lead to an unsteady behaviour of the end-to-end distance. In fact, a steady state is reached within relatively short times upon fiber injection into the flow. We also examined the tensile and bending forces acting on the individual elements into which fibers are discretized. These forces are higher for longer fibers, indicating a stronger action of stretching and bending of the fiber's major symmetry axis exherted by the fluid.

As far as bending is concerned, the most relevant future development of the present work is the inclusion of bending rigidity effects in the equations of fiber motion. In particular, the inclusion of an internal resistance torque will allow a more realistic representation of fiber bending dynamics by taking into account the existence of an equilibrium conformation, and measuring the energy to be transferred from the fluid to the fibers in order to deviate from such conformation. Since fiber bending is ultimately controlled by the hydrodynamic fluid-fiber interaction, and a dependency on the flow Reynolds number is expected, another development will be the study of Reynolds numbers effects by performing simulations at Re_τ much larger than the single value considered here.

Finally, it would be interesting to examine wether or not flexible fibers in wall-bounded turbulence tend to align preferentially with the direction of the strongest Lagrangian fluid stretching, as already observed for the case of rigid fibers [34, 36, 51].

Compliance with ethical standards

Conflict of interest The authors declare that they have no conflict of interest.

References

1. Allende S, Henry C, Bec J (2018) Stretching and buckling of small elastic fibers in turbulence. Phys Rev Lett 121:154501
2. Andrić J, Fredriksson ST, Lindström SB, Sasic S, Nilsson H (2013) A study of a flexible fiber model and its behavior in DNS of turbulent channel flow. Acta Mech 224:2359
3. Andrić J, Lindström SB, Sasic S, Nilsson H (2014) Rheological properties of dilute suspensions of rigid and flexible fibers. J Non-Newton Fluid Mech 212:36
4. Boer L, Buist KA, Deen NG, Padding JT, Kuipers JAM (2018) Experimental study on orientation and de-mixing phenomena of elongated particles in gas-fluidized beds. Powder Technol 329:332
5. Borgnino M, Gustavsson K, De Lillo F, Boffetta G, Cencini M, Mehlig B (2019) Alignment of non-spherical active particles in chaotic flows. Phys Rev Lett (Accepted paper)
6. Bounoua S, Verhille G, Bartoli A (2018) Tumbling of inertial fibers in turbulence. Phys Rev Lett 121:124502
7. Brenner H, Cox RG (1963) The resistance to a particle of arbitrary shape in translational motion at small Reynolds numbers. J Fluid Mech 17:561
8. Brenner H (1964) The Stokes resistance of an arbitrary particle IV. Arbitrary fields of flow. Chem Eng Sci 19:703
9. Brouzet C, Verhille G, Le Gal P (2014) Flexible fiber in a turbulent flow: a macroscopic polymer. Phys Rev Lett 112:074501
10. Byron M, Einarsson J, Gustavsson K, Voth G, Mehlig B, Variano E (2015) Shape-dependence of particle rotation in isotropic turbulence. Phys Fluids 27:035101
11. Clift R, Grace JR, Weber ME (1978) Bubbles, drops and particles. Academic Press, New York
12. Cox RG (1971) The motion of long slender bodies in a viscous fluid. Part 2. Shear flow. J Fluid Mech 45:625
13. Dotto D, Marchioli C (2019) Orientation, distribution and deformation of inertial flexible fibers in turbulent channel flow. Acta Mech 230:597–621

14. Fan FG, Ahmadi G (1995) A sublayer model for wall deposition of ellipsoidal particles in turbulent streams. J Aerosol Sci 25:831
15. Gay A, Favier B, Verhille G (2018) Characterisation of flexible fibre deformations in turbulence. Europhys Lett 123:24001
16. Gustavsson K, Jucha J, Naso A, Lévêque E, Pumir A, Mehlig B (2017) Statistical model for the orientation of non-spherical particles settling in turbulence. Phys Rev Lett 119:254501
17. Hinch EJ, Leal LG (1979) Rotation of small non-axisymmetric particles in a simple shear flow. J Fluid Mech 92:591
18. Hunt JCR, Wray A, Moin P. Eddies, stream, and convergence zones in turbulent flows. Center for Turbulence Research Report, CTR-S88
19. Jeffery GB (1922) The motion of ellipsoidal particles immersed in a viscous fluid. Proc R Soc Lond Ser A 102:161
20. Joung CG, Phan-Thien N, Fan XJ (2001) Direct simulation of flexible fibers. J Non-Newton Fluid Mech 99:1
21. Kim S, Karrila SJ (1991) Microhydrodynamics: principles and selected applications. Butterworth-Heinemann, Stoneham
22. Kunhappan D, Harthong B, Chareyre B, Balarac G, Dumont PJJ (2017) Numerical modelling of high aspect ratio flexible fibers in inertial flows. Phys Fluids 29:093302
23. Lindström SB, Uesaka T (2008) Particle-level simulation of forming of the fiber network in papermaking. Int J Eng Sci 46:858
24. Lindström SB, Uesaka T (2007) Simulation of the motion of flexible fibers in viscous fluid flow. Phys Fluids 19:113307
25. Lovecchio S, Zonta F, Marchioli C, Soldati A (2017) Thermal stratification hinders gyrotactic micro-organism rising in free-surface turbulence. Phys Fluids 29:053302
26. Lovecchio S, Marchioli C, Soldati A (2013) Time persistence of floating particle clusters in free-surface turbulence. Phys Rev E 88:033003
27. Lundell F, Soderberg LD, Alfredsson PH (2011) Fluid mechanics of papermaking. Annu Rev Fluid Mech 43:195
28. Marchioli C, Zhao L, Andersson HI (2016) On the relative rotational motion between rigid fibers and fluid in turbulent channel flow. Phys Fluids 28:013301
29. Marchioli C, Soldati A (2013) Rotation statistics of fibers in wall shear turbulence. Acta Mech 224:2311
30. Marchioli C, Fantoni M, Soldati A (2010) Orientation, distribution, and deposition of elongated, inertial fibers in turbulent channel flow. Phys Fluids 22:033301
31. Martínez M, Vernet A, Pallares J (2017) Clustering of long flexible fibers in two-dimensional flow fields for different Stokes numbers. Int J Heat Mass Transf 111:532
32. Mashayekhpour M, Marchioli C, Lovecchio S, Nemati Lay E, Soldati A (2019) Wind effect on gyrotactic micro-organism surfacing in free-surface turbulence. Adv Water Resour 129:328–337
33. Moffet RC, Prater KA (2009) In-situ measurements of the mixing state and optical properties of soot with implications for radiative forcing estimates. Proc Natl Acad Sci 106:11872
34. Ni R, Ouellette NT, Voth GA (2014) Alignment of vorticity and rods with Lagrangian fluid stretching in turbulence. J Fluid Mech 743:R3
35. Ni R, Kramel S, Ouellette NT, Voth GA (2016) Measurements of the coupling between the tumbling of rods and the velocity gradient tensor in turbulence. J Fluid Mech 766:202–225
36. Parsa S, Guasto JS, Kishore M, Ouellette NT, Gollub JP, Voth GA (2011) Rotation and alignment of rods in two-dimensional chaotic flow. Phys Fluids 23:043302
37. Niazi Ardekani M, Brandt L (2019) Turbulence modulation in channel flow of finite-size spheroidal particles. J Fluid Mech 859:887
38. Picciotto M, Marchioli C, Soldati A (2005) Characterization of near-wall accumulation regions for inertial particles in turbulent boundary layers. Phys Fluids 17:098101
39. Ravnik J, Marchioli C, Soldati A (2018) Application limits of Jeffery's theory for elongated particle torques in turbulence: a DNS assessment. Acta Mech 229:827
40. Rosti ME, Banaei AA, Brandt L, Mazzino A (2018) Flexible fiber reveals the two-point statistical properties of turbulence. Phys Rev Lett 121:044501
41. Sabban L, Cohen A, van Hout R (2017) Temporally resolved measurements of heavy, rigid fibre translation and rotation in nearly homogeneous isotropic turbulence. J Fluid Mech 814:42
42. Sabban L, van Hout R (2011) Measurements of pollen grain dispersal in still air and stationary, near homogeneous, isotropic turbulence. J Aerosol Sci 42:867
43. Shapiro M, Goldenberg M (1993) Deposition of glass fiber particles from turbulent air flow in a pipe. J Aerosol Sci 24:65
44. Verhille G, Bartoli A (2016) 3D conformation of a flexible fiber in a turbulent flow. Exp Fluids 57:117
45. Voth GA, Soldati A (2017) Anisotropic particles in turbulence. Annu Rev Fluid Mech 49:249
46. Xiang P, Kuznetsov AV (2008) Simulation of shape dynamics of a long flexible fiber in a turbulent flow in the hydro-entanglement process. Int Commun Heat Mass Transf 35:529
47. Yamamoto S, Matsuoka T (1993) A method for dynamic simulation of rigid and flexible fibers in a flow field. J Chem Phys 98:644
48. Zhan C, Sardina G, Lushi E, Brandt L (2014) Accumulation of motile elongated micro-organisms in turbulence. J Fluid Mech 739:22
49. Zhang D, Smith DE (2016) Dynamic simulation of discrete fiber motion in fiber-reinforced composite materials processing. J Compos Mater 50:1301
50. Zhao L, Gustavsson K, Ni R, Kramel S, Voth G, Mehlig B. Orientation patterns of non-spherical particles in turbulence. arXiv:1707.06037v2 [physics.flu-dyn]
51. Zhao L, Andersson HI (2016) Why spheroids orient preferentially in near-wall turbulence. J Fluid Mech 807:221
52. Zhao L, Challabotla NR, Andersson HI, Variano EA (2019) Mapping spheroid rotation modes in turbulent channel flow: effects of shear, turbulence and particle inertia. J Fluid Mech 876:19